Physica B 671 (2023) 415454

Contents lists available at ScienceDirect

Physica B: Condensed Matter

journal homepage: www.elsevier.com/locate/physb

Switchable multifunctional meta-structure employing vanadium dioxide in the terahertz range

Ru-Jia Cao, Zhen Qiao, You Lv, Hai-Feng Zhang [*]

College of Electronic and Optical Engineering & College of Flexible Electronics (Future Technology), Nanjing University of Posts and Telecommunications, Jiangsu province, 210023, China

ARTICLE INFO

Keywords:
Electromagnetically induced transparency
Electromagnetically induced absorption
Meta-structure
Terahertz
Vanadium dioxide

ABSTRACT

A meta-structure (MS) that can realize a conversion between electromagnetically induced transparency (EIT) and electromagnetically induced absorption (EIA) in the Terahertz (THz) range by utilizing phase-transition vanadium dioxide (VO_2) has been reported. This work is controlled by temperature to change the conductivity of VO_2 to achieve the switching function. When the VO_2 is in the insulator state, the MS is designed to achieve EIT based on the principle of bright mode near-field coupling bright mode. The EIT behavior owns a peak of 0.8 at 0.430 THz with a maximum group delay of up to 6.5 ps. The MS behaves the function of EIA accompanied by the maximum absorption rate of 93.8 % at 0.432 THz while the VO_2 film is tuned to the metallic state. The reason for the EIA phenomenon is the magnetic effect of the magnetic dipole generated by the MS in the coupling process. The observed EIT and EIA effects are both theoretically explained by the classic two-oscillator model. In addition, the air columns of the dielectric substrate are utilized for the purpose of frequency approaching. This proposed MS provides a new idea for the design of non-contact regulation and reconfigurable and highly absorbent MSs.

1. Introduction

Terahertz (THz) waves are EM waves with frequencies in the range of 0.1–10 THz which occupy an extraordinarily particular position in the electromagnetic spectrum, coinciding with millimeter waves in the long wavelength band and infrared waves in the short wavelength band. Located in the transition zone from electronics to photonics, THz technology has exhibited abundant applications, such as THz shielding [1], DNA detection [2], THz imaging [3,4], THz communication [5], radar [6], and so on. However, it is difficult to devise THz devices based on conventional methods, which greatly limits the further development and actual application of THz technology. MSs [7] are new artificial materials with unusual EM properties [8], which include metamaterials and metasurfaces. The electrical permittivity and magnetic permeability of MSs can be negative instead of usual natural materials. Consequently, as novel materials made up of subwavelength unit cell arrays, MSs have access to realize functions that cannot be realized by natural materials. They can be employed for manipulating electromagnetic waves, which provides a new idea and way for the design of terahertz devices.

Electromagnetically induced transparency (EIT) is a quantum interference phenomenon observed in atomic or molecular systems based on destructive interference, which enables the original wide absorption band of the medium to present a steep narrow transmission peak [9]. EIT produces strong dispersion within the transparency window, which brings about slow light effects and enhanced nonlinear magnetization, thus it has broad application prospects in quantum memory [10], quantum information processing [11], quantum precision measurement [12], etc. The successful realization of the EIT effect requires exceedingly demanding experimental conditions with low temperature and high-intensity laser, which is not easy to achieve. The researchers started to be committed to studying the EIT phenomenon in MSs until Zhang et al. [13] first achieved plasmon-induced transparency which is similar to the EIT effect in MSs without strict experimental conditions in 2008. Some people use miscellaneous structures and materials to realize the phenomenon of EIT. For instance, Wang et al. [14] presented a planar plasmonic metamaterial consisting of nanoring and nanorod compound structures for EIT and slow light characteristics in 2013. Li et al. [15] in 2015 designed a metamaterial EIT structure composed of cut wire and asymmetric split-ring resonators. Also, Loke et al. [16] proposed a high-performance optical modulator with a double-layer graphene-based metasurface that can support a high-quality factor resonance based on the EIT in 2022. So far, the studies that the EIT is combined

---

* Corresponding author.
E-mail addresses: hanlor@163.com, hanlor@njupt.edu.cn (H.-F. Zhang).

https://doi.org/10.1016/j.physb.2023.415454
Received 1 September 2023; Received in revised form 6 October 2023; Accepted 23 October 2023

with others such as graphene MSs [17,18], MSs sensors [19], polarization conversions [20], etc, have arisen widespread interest at home and abroad.

Similar to EIT, electromagnetically induced absorption (EIA) is also an interference phenomenon of a four-level atomic system which is antagonistic to EIT for its name. The constructive interference of different excitation pathways results in EIA. EIA has a wide range of practical applications in narrowband filters [21], absorbers [22], and optical modulators [23]. Recently, several groups [24–26] have observed EIA behavior based on MSs. Since EIT and EIA are similar in terms of implementation, combining them in the same device can save material costs to achieve multifunctional device functions. In 2018, Cao et al. [23] proposed a graphene-based tunable EIA that used a pair of nanorods coupled to a ring resonator to obtain the EIT phenomenon. Simultaneously, they applied Babinet's principle to transform the EIT into EIA. In 2022, Lu et al. [27] designed an EIT based on circularly polarized waves to achieve the transition from EIT to EIA by changing the conductivity of the phase change material vanadium dioxide (VO_2). Nevertheless, the EIA absorption rates of the above studies are insufficient and it is not convenient to operate the regulation function of the EIT-EIA conversion process.

MS-based designs are mostly static and always have a single function. Nowadays, integrated multifunctional devices are emerging, which have attracted attention for they concentrate a variety of functions to optimize the system as a whole and have multiple functions as well as system flexibility. So the design and research of multifunctional MSs are crucial. In 2012, Liu et al. [28] first reported meta-material based on VO_2 in THz field. VO_2 is a metal oxide with phase transition properties. The phase transition of VO_2 from the insulator state to the metallic state can be achieved by heat [29], electricity [30], and light [31]. The conductivity of VO_2 can change by four to five orders of magnitude during its transition from the insulating to the metallic state [32], making it extremely attractive for the implementation of switchable and tunable multifunctional THz devices. VO_2 offers the advantages of easy manufacturing and low cost. Controlled by temperature, the VO_2 is usually utilized in MS for the implementation and control of the EIT. For example, Chen et al. [33] obtained a low-loss polarization-insensitive EIT MS with VO_2 in 2020. The EIT windows and slow-light effect can be manipulated dynamically by varying the conductivity of VO_2. Furthermore, multi-functional THz MSs that can achieve EIT and other functions by adjusting the state of VO_2 are obtainable [34–36]. In 2022, the frequency and amplitude tunable meta-surfaces based on VO_2 were realized [37], which helps to realize active meta devices for THz domain. Not least because the VO_2 can be dominated by temperature, this means that just changing the temperature of the environment to regulate the conductivity of VO_2 can achieve a state transition. This non-contact regulation can simplify experimental complexity, enhance operability, improve safety, and provide the possibility for future artificial intelligence to replace researchers in experimental operations. However, there are many shortcomings in the current structural design of MSs, such as complex structure, single function, insufficient absorption rate, and complicated regulation methods.

Herein, a THz MS based on VO_2 with EIT and EIA is presented. The MS is made up of an H-shaped resonator, square ring resonator, VO_2 film, and silicon dioxide dielectric substrate with air columns. When the VO_2 film is in the insulating phase at a room temperature of 25 °C, an EIT window with maximum transmittance reaching 80 % at 0.430 THz can be observed. The group delay of the EIT is up to 370 ps. The H-shaped resonator, and the square ring resonator are both bright modes, the coupling of which arises the EIT. When VO_2 transforms into its fully metallic phase, the EIT functionality will be switched off and instead, the MS has the function of absorbing with a max absorption exceeding 93.8 % at 0.432 THz. The magnetic effect that the VO_2 film, the H-shaped resonator and the square ring resonator caused gives rise to the EIA effect. By regulating the conductivity of VO_2 through varying the temperature, EIT and EIA can be switched freely. The classic "dual harmonic oscillator" coupling model explains the EIT and EIA phenomena. Moreover, the current and electric field distribution diagrams are provided for further analysis. The difference between EIT and EIA resonant frequencies is reduced by placing air columns in the dielectric substrate. This work shows good prospects for multifunctional switching devices, absorption filters, non-contact modulation devices, and slow-light devices.

2. Structural design and simulated results

2.1. MS unit design

As observed in Fig. 1a, the schematic diagram of the periodic arrangement of the design MS is demonstrated. The MS is periodically placed along the x-axis and the y-axis. The waves where the electromagnetic field is parallel to the y-axis are vertically incident on the surface of the MS from the -z-axis. The structure consists of three portions with dissimilar materials in Fig. 1b. The top layer as shown in Fig. 1c is composed of an H-shaped structure and a square ring structure whose outer frame length is a_1 and width is b_1. The square ring structure and H-shaped resonator are both made of gold with a conductivity of 4.561 × 107 S·m-1 [38] and its thickness D_1 is 0.02 μm and are set on a silicon substrate (loss-free) with a permittivity of 11.9 [39]. Fig. 1d displays the structure of the silicon substrate, which takes $P = 160$ μm as the side length with a thickness $D_2 = 35$ μm. Air column structures are combined into a silicon substrate just as revealed in Fig. 1d. The diameter of the inner circle air column is designed as $R_1 = 8.7$ μm and the outer circle air column is $R_2 = 9.5$ μm. It can be seen that the VO_2 structure is designed into a meander line structure which is vertically curved in the right half part of the VO_2 film from the top view and its thickness $D_3 = 2$ μm in Fig. 1e. The parameters m and n can be obtained from the equations $m = a_2/2$ and $n = x\text{-}2 \times b_2$. Moreover, other detailed and comprehensive dimensional information has been given in Table 1. When the VO_2 is set to the insulator state the conductivity of which is 200 S/m, which corresponds to the temperature of about 25 °C [40], the MS enables the function of EIT. Once the external temperature is higher than the critical temperature of 68 °C [27], the VO_2 will change from an insulating state to a metallic state and its conductivity can reach 300, 000 S/m [41]. Simultaneously, the MS is capable of fulfilling the performance of EIA.

2.2. The appearance of the EIT phenomenon

As mentioned above, EIT, a kind of phenomenon in quantum physics and the result of energy level interference, is possible under strict experimental conditions. Therefore, MSs are employed for EIT behavior. Generally, there are three coupling mechanisms for simulating EIT in MSs. The first one is that the EIT effect can be induced by the coupling of bright modes and dark modes [42]. The second one is that it can be achieved by the coupling between bright modes [43], and the another one is the coupling of bright modes and quasi dark modes [44]. Compared to the bright mode, which has a large dipole moment, the dark mode has an almost negligible dipole moment and cannot be directly excited by the incident electromagnetic field. As a result, the electromagnetic field can directly stimulate the bright mode but not the dark mode. The EIT effect realized through the coupling of bright mode and the bright mode was initially observed in the asymmetric open ring periodic structure [45]. Under the excitation of the applied electromagnetic field, both the upper and lower splitting arcs of the open ring can directly couple the energy of the electromagnetic field, forming two bright modes. The coupling of the two bright modes can excite the reverse current to contribute to an EIT with a high Q value.

In this paper, an H-shaped structure and square ring structure are designed for EIT which is based on bright mode coupled with bright one. The incident polarization waves can directly excite the square ring structure, which is defined here as a bright resonator 1. Moreover, the H-

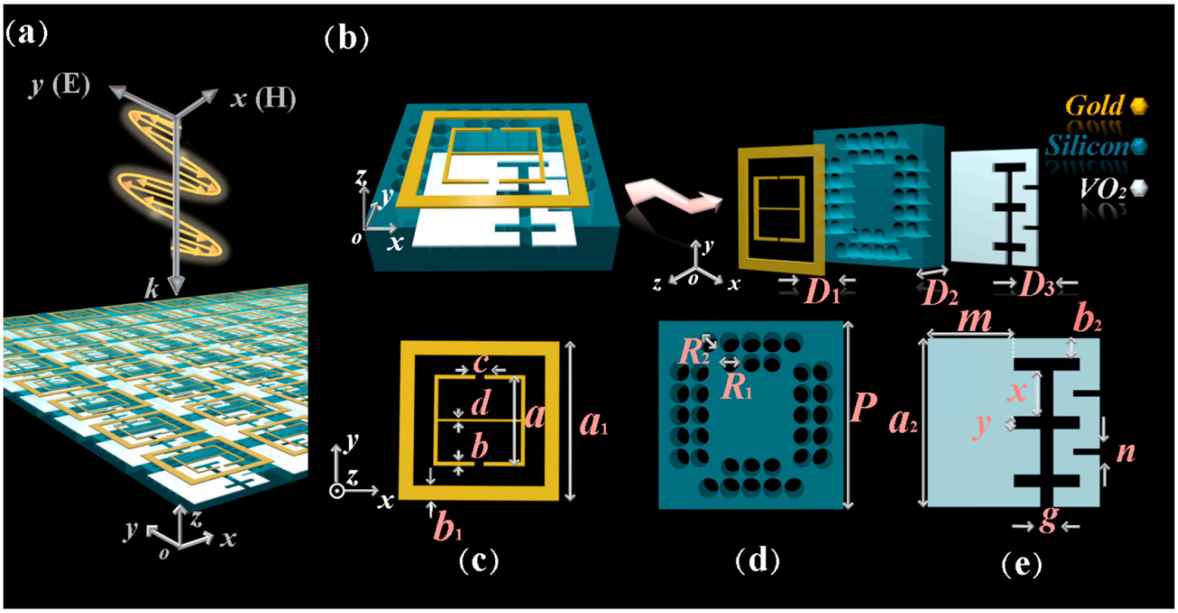

Fig. 1. (a) Schematic diagram of periodic arrangement of the designed MS, (b) the stereoscopic view of the presented MS and three-layer structure, (c) the top view of the module that can realize the EIT, (d) the top view of the design of the dielectric substrate, and (e) the top view of the module that can realize the EIA.

Table 1
The detailed geometric dimensions of the MS unit.

Parameters	Value (μm)	Parameters	Value (μm)	Parameters	Value (μm)
D_1	0.02	a	80	c	2
D_2	35	b	7	d	2
D_3	2	a_1	138	g	5
P	160	b_1	25	x	35
R_1	17.4	a_2	130	y	10
R_2	19.0	b_2	15		

shaped structure can also be directly excited by the incident polarization waves, which is bright resonator 2. It is the weak hybridization between the bright resonators 1 and 2 with frequency detuning that gives birth to the EIT in MSs [46]. When the VO_2 film is in the state of insulating, an EIT window is observed in the range from 0.30 THz to 0.54 THz and the transmission peak is up to 0.801 at 0.430 THz. Furthermore, it can be seen from Fig. 2 that transmission dips frequencies are 0.345 THz and 0.512 THz, and the corresponding points are marked in the picture below.

Concurrently, the resonators 1 and 2 are respectively simulated as illustrated in Fig. 2, for a deep insight into the physical principle therein. It can be observed from Fig. 2a and b that the two resonators are both directly excited by the incident waves and behave transmission responses. The resonator 1 has a transmission dip at 0.357 THz (P' point in Fig. 2a) and the transmission dip of the resonator 2 is at 0.508 THz (Q' point in Fig. 2b). When the two resonators are combined together as displayed in Fig. 2c, the weak hybridization between the two bright modes with frequency detuning contributes to the transmission maximum peak of 0.801 at 0.430 THz (M point in Fig. 2c). The left transmission dip P point at 0.45 THz in Fig. 2c is corresponding to the P' point in Fig. 2a. The right transmission dip Q point at 0.512 THz in Fig. 2c is in the corresponding way of the Q' point in Fig. 2b.

Further, Fig. 3 shows the surface current distributions of the bright mode resonator 1 and the bright mode resonator 2 at different frequencies. It can be seen in Fig. 4a that at the left transmission dip of 0.345 THz, the resonator 1 can be excited via the incident waves where the electric field is along the y-direction and the surface currents mainly concentrate on the two sides of the resonator 1 which are parallel to the y-axis. The dominant current direction is along the y-axis and the current intensity inside the ring is stronger than that outside the ring. At the right transmission of 0.512 THz in Fig. 4b, the resonator 2 can be excited via the incident waves, the surface currents are concentrated and distributed on the arms of the resonator 2 which are parallel to the y-axis. The main current of the resonator is along the -y-axis. It is obvious that the excited-dominated currents of the two resonators are in opposite directions and the current intensity of the resonator 2 is much stronger than the resonator 1. When the two resonators are combined, the surface current distribution is illustrated in Fig. 3c. It can be observed that the two resonators generate opposite currents at 0.430 THz and the two resonators' main current directions are exchanged compared to Fig. 3a and b. The destructive interference coupling between the two bright modes is the reason for the formation of EIT behavior.

To have a deeper understanding of the EIT phenomenon based on MSs, the classical three-level atomic system will be employed to explain [27]. It can be seen from Fig. 4, there are three states in the three energy level atomic system, which are ground state $|0>$ and two excited states $|1>$ and $|2>$. Additionally, the Ω_1 and Ω_2 stand for the phases of two transition channels, and the γ_1 and γ_2 refer to the coupling coefficients between energy levels. When a probing light is incident on a material with a three-energy level atomic system, the atom will leap from the ground state $|0>$ to the excited state $|1>$ ($|0>\rightarrow|1>$) accompanied by radiate under the condition that the frequency of the probing light and the atomic leap is consistent. Consequently, the probing light is completely absorbed and the transmittance is close to zero. Next, a stronger coupling light is added to the system when keeping the intensity of the probing light constant which will result in a change in the energy level position, allowing another leap path $|0>\rightarrow|1>\rightarrow|2>\rightarrow|1>$ for the particle to occur. The different paths of the transition produce destructive interference, leading to a decrease in the ability to absorb probing light. Thus, probing light turns into transparent at its original absorption peak and that is what we called 'EIT'. In this model, when incident waves are vertically incident on the MS, the incident waves interact with the resonator 1 to form a bright mode. The excitation process $|0>\rightarrow|1>$ is called path 1. The resonator 2 can interact with the incident wave too, thus forming excitation path 2 ($|0>\rightarrow|1>\rightarrow|2>\rightarrow|1>$). At the resonant frequency, when there is a phase difference of Π between path 1 and path 2, the two paths will interfere with each other,

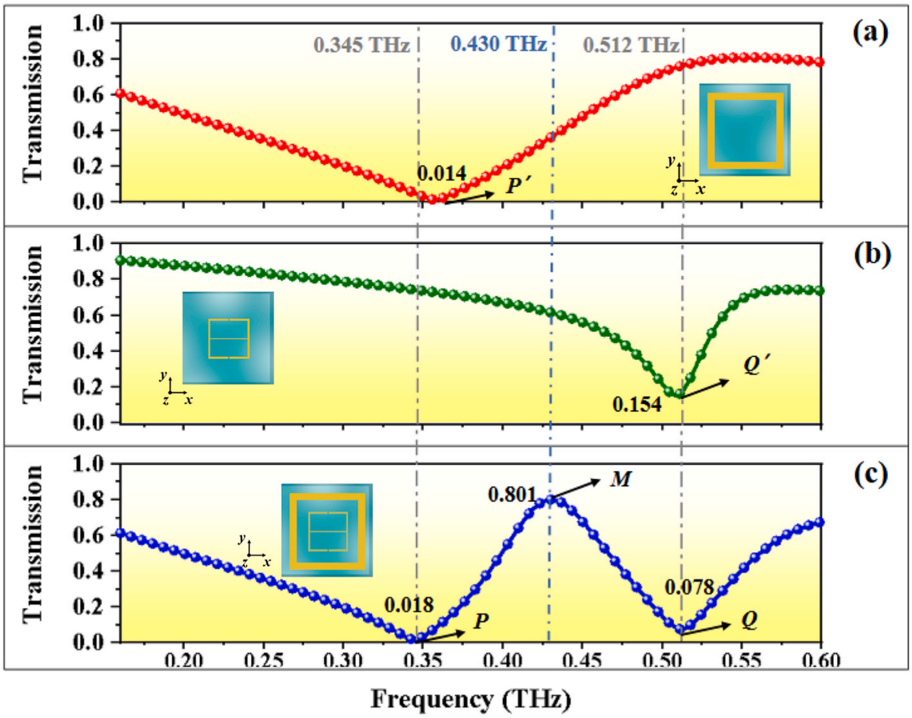

Fig. 2. (a) The corresponding transmission response of the resonator 1, (b) the transmission spectrum of the resonator 2, (c) the transmission spectrum of the combination of the two resonators when the conductivity of VO_2 is 200 S/m.

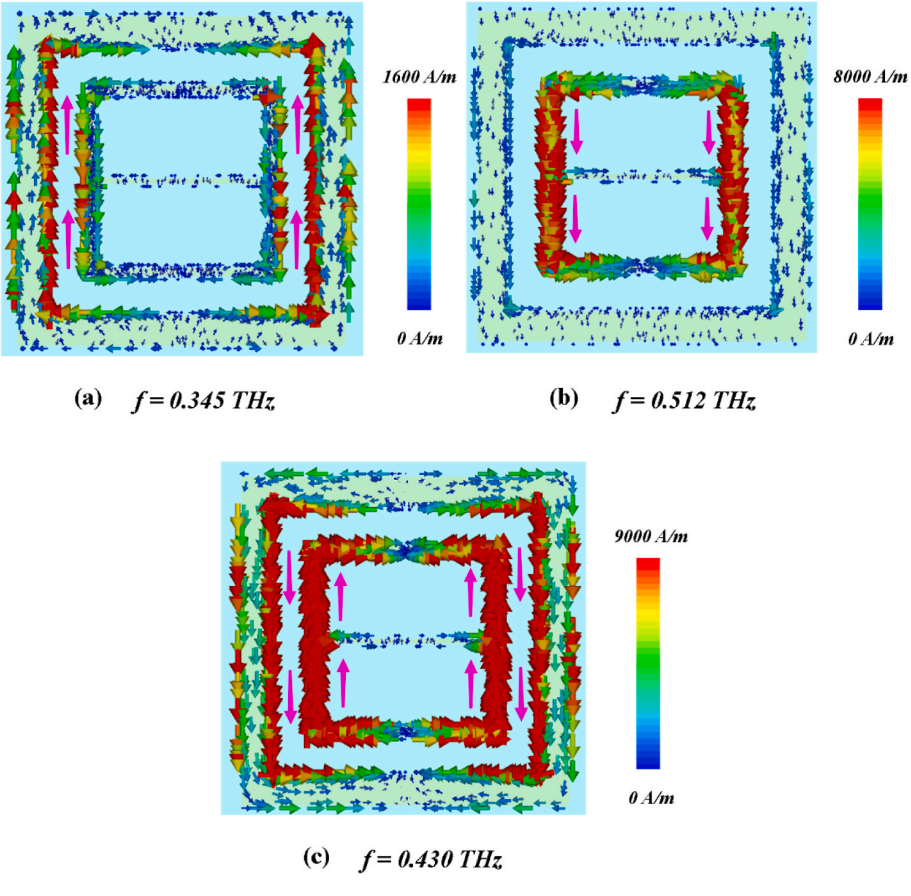

Fig. 3. The surface current distributions for the combination of resonators 1 and 2 in Fig. 1c at (a) 0.345 THz, (b) 0.512 THz, (c) 0.430 THz when the VO_2 is in the insulating state.

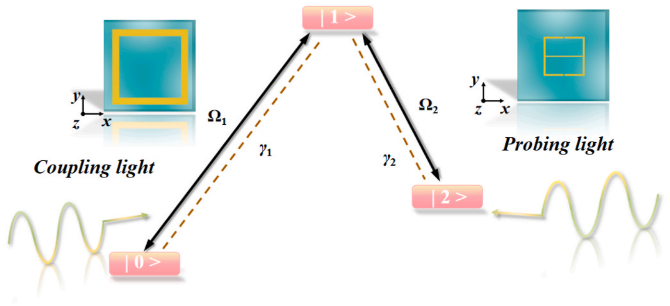

Fig. 4. The comparison of the coupling mechanism between the classical three-level atomic system and the EIT MS.

therefore generating the EIT phenomenon.

Within the EIT window, the transmission phase undergoes a phase abrupt change at the frequency point corresponding to the transmission peak accompanied by a strong dispersion phenomenon, which results in the large group index (n_g) in the transmission band and behaves the slow light effect. The group delay is employed to show the slow light characteristics of the EIT behavior, which is calculated as follows [27]:

$$t_{GD} = -\frac{d\varphi}{d\omega} \tag{1}$$

Where φ represents the phase and ω refers to the angular frequency. Furthermore, the n_g of EIT is also figured out using the following formula [27]:

$$n_g = \frac{c}{t} t_{GD} \tag{2}$$

where c is the speed of light and t stands for the thickness of the cell structure. Fig. 5a demonstrates the abrupt changes in the transmission phase in the range of 0.30 THz to 0.540 THz. Besides, it can be noted that the value of the maximal group delay for the EIT window is 6.5 ps and the maximum n_g is close to 523. This indicates that the design provides a good slow light effect.

2.3. The appearance of the EIA phenomenon

The EIA phenomenon can be observed in the original EIT window when the VO_2 is in a metallic state. As observed in Fig. 6a, b and c, VO_2 films were designed as two symmetrically distributed split resonant rings, which is defined as structure I. The two resonant rectangular rings with opposite opens are in the middle of the silicon substrate. The specific parameters of structure I are as follows in Table 2. As can be seen from Fig. 6d, when the VO_2 is in the insulator state, the transmission peak of the EIT was 0.85 at 0.327 THz. While the VO_2 is in the metallic state, an absorption peak that was up to 0.96 could be observed at 0.410 THz. Although the EIA phenomenon was obvious, the resonance frequencies of the EIT and EIA behavior of structure I as illustrated by Fig. 6d do not correspond.

Nevertheless, it is crucial to tune EIT and EIA to the same frequency so that the function selection at a certain frequency can be achieved for more precise control. To improve the frequency difference between the EIT peak and the EIA peak, some parameters related to the VO_2 were changed in a reasonable range and the results are exhibited in Fig. 7. It can be found from Fig. 7a that as the length of the rectangular ring e increases, the frequency point of the EIA shifts to the direction in which the frequency decreases. When the parameter e was 130 μm, the corresponding frequency is at about 0.410 THz. However, the change in the width of the rectangular ring f has a large effect on the absorption spectra. It is not hard to see in Fig. 7b that the larger the value of f, the better effect of the EIA. Due to the size limitation of the silicon substrate, the maximum value of f cannot exceed 70 μm. As f varies from 40 μm to 68 μm, the absorption gets higher and the peak frequency of the EIA shifts to the direction in which the frequency decreases. Fig. 7c shows the value of the opening size of the resonant rectangular ring i makes little difference to frequency shift. When the parameter i changes from 1 μm to 15 μm, the peak frequency of the EIA changes about 0.01 THz. And Fig. 7d displays that with the increase of h, the peak frequency will move to the direction in which the frequency increases and the peak is changed simultaneously. Ultimately, the parameters are selected as follows: $e = 126$ μm, $f = 68$ μm, $i = 10$ μm, $h = 20$ μm. The difference between the EIT peak and EIA peak frequencies remains unresolved.

In the primary stage of optimization, the resonant rings in structure I were replaced by the meander line in structure II for the decrease of the difference of frequency between EIT and EIA, which is displayed in Fig. 8. The meander line is located in the left half part of the VO_2 structure and the bend angle of it is 90°, as is exhibited in Fig. 8d. It can be seen from Fig. 8f that the peak frequency of the EIT is 0.329 THz with the maximum value of 0.8 when the VO_2 is in the insulating state. The peak frequency of the EIA behavior is 0.370 THz with a maximum absorption of 0.96 while the VO_2 is in its metallic state. It can be found that the frequency difference is reduced from 0.083 THz at the beginning to 0.041 THz by comparing Fig. 8e with Fig. 8f. It has to be noted that not only the structure of the VO_2 film was changed, but other structural parameters were also adjusted in the process of the model evolution. Owing to the limitation of space, the intermediate process parameter changes will not be repeated, only the final model parameters are given.

From the above, based on structure II, some air columns are punched through the silicon dielectric substrate as shown in Fig. 9a and b and that is structure III. Arranged around the substrate, the air columns have two rows, inner and outer, with diameters R_1 and R_2. And the number and radius of the air columns can influence the resonant frequencies of both EIT and EIA, which makes a difference in the frequency difference of the EIT and EIA. When the parameters of the air column are adjusted to a suitable value, the two frequencies can be achieved close to each other as revealed in Fig. 9c. The R_1 and R_2 are 17.4 μm and 19.0 μm. Other parameters of the model are set as shown in Table 1. The EIT the

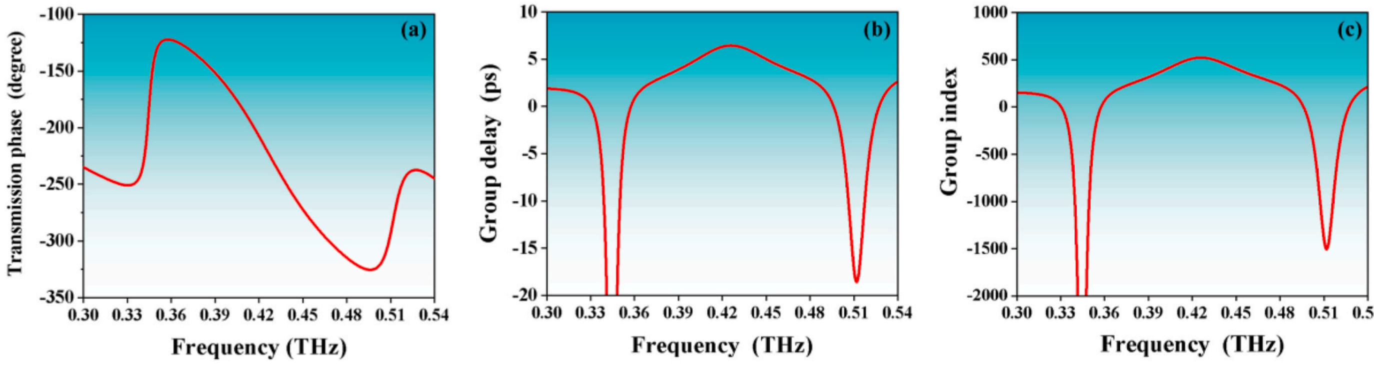

Fig. 5. For the EIT: (a) the transmission phase, (b)the group delay, (c)the group index.

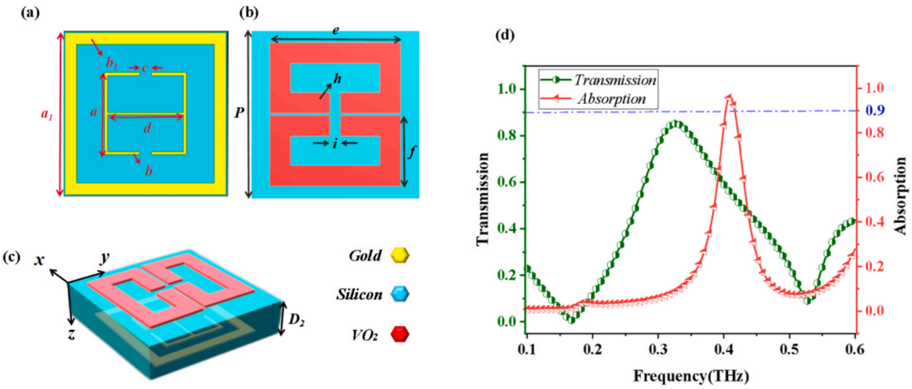

Fig. 6. (a)The top and (b) bottom view of the structure I which was initially designed.(c)The structure diagram of the structure I.(d)The transmission and absorption spectra of structure I when the VO_2 film is in the insulator state and metallic state separately.

Table 2
The detailed geometric dimensions of structure I

Parameters	Value (μm)	Parameters	Value (μm)	Parameters	Value (μm)
P	140	***a***	70	***b***	5
***D*₁**	0.02	***a*₁**	138	***b*₁**	20
***D*₂**	35	***e***	126	***f***	68
***D*₃**	2	***h***	20	***i***	10
c	10	***d***	2		

resonant frequency of which is at 0.430 THz can be achieved when VO_2 is insulated, and once the VO_2 is metallic, the design can achieve EIA with a peak of 0.938 at 0.432 THz. The frequency difference between the EIT and the EIA is 0.002 THz, which meets the requirements for design. The final EIA behavior is shown in Fig. 9c (the red curve *A*).

Additionally, the transmission and reflection spectra as well as the absorption spectra for the resonator 1, the resonator 2, the combination of the resonators 1 and 2, and the individual VO_2 structure are given in Fig. 10. The absorption of the proposed MS can be acquired through the equation [47].

$$A = 1 - \left|T_{21}{}^2\right| - \left|R_{21}{}^2\right| - \left|T_{11}{}^2\right| - \left|R_{11}{}^2\right|$$

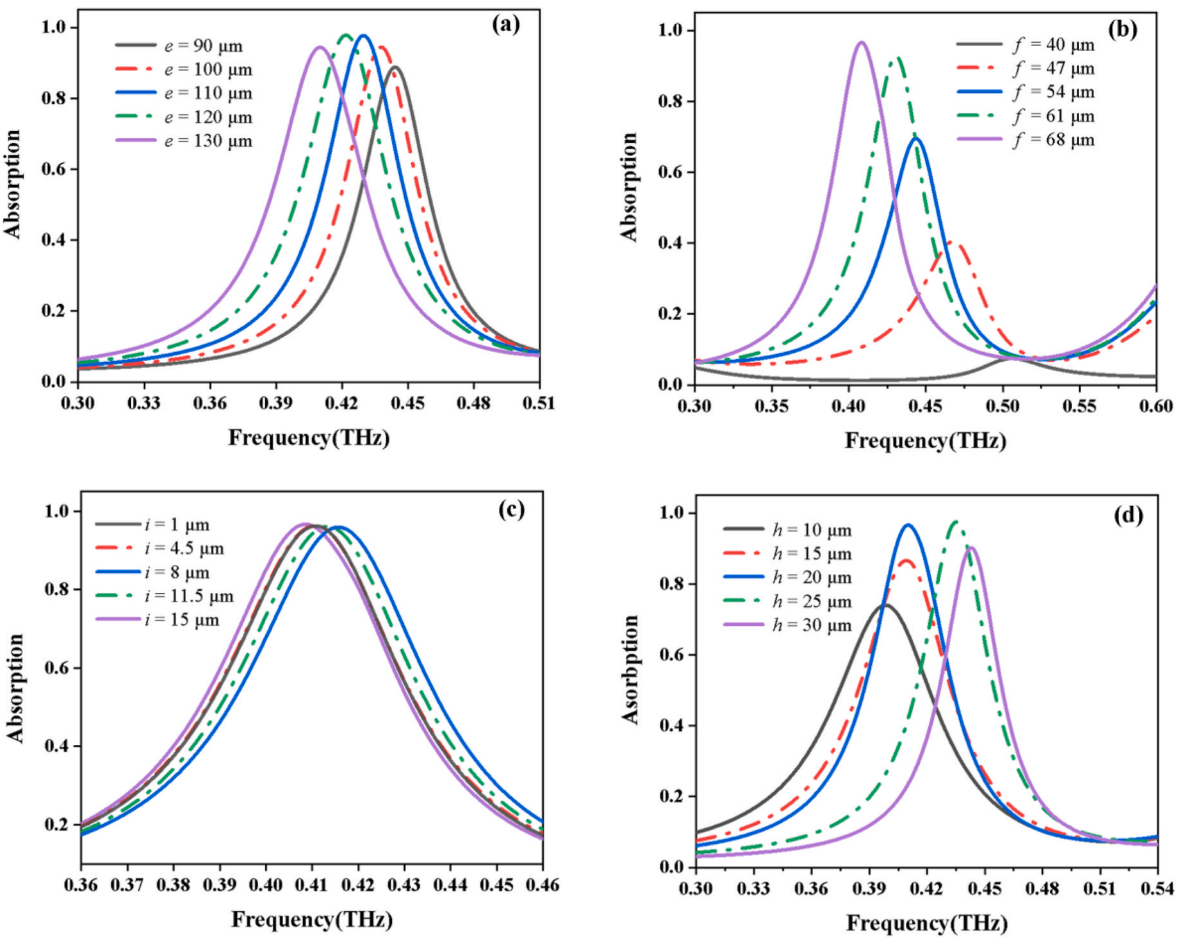

Fig. 7. The absorption spectra as a function of (a) *e*, (b) *f*, (c) *i* and (d) *h* when VO_2 is in the metallic state.

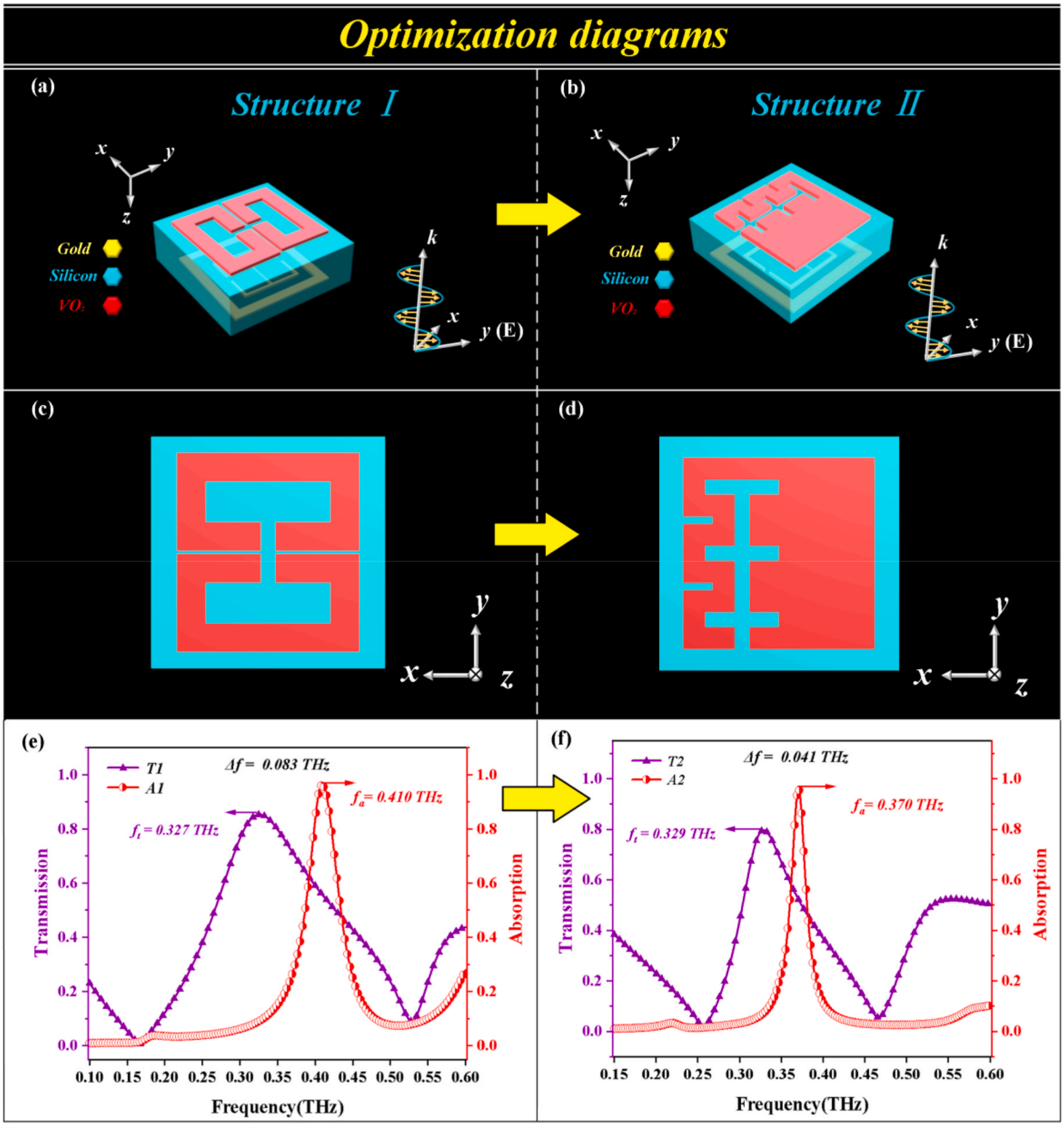

Fig. 8. (a) The perspective view of structure I, (b) the perspective view of structure II,(c) the bottom view of structure I, (d) the bottom view of structure II, (e) the transmission curve (*T1*) of the structure I when VO_2 is in the insulating state and the absorption curve (*A1*) of the structure I when VO_2 is in the metallic state, (f) the transmission curve (*T2*) of the structure II when VO_2 is in the insulating state and the absorption curve (*A2*) of the structure II when VO_2 is in the metallic state.

Where T_{11} and T_{21} refer to the transmission coefficients of the main polarization and polarization conversion. And R_{11} and R_{21} refer to the reflection coefficients of the main polarization and polarization conversion. As shown in Fig. 10, the transmission coefficients of polarization conversion T_{21} and the reflection coefficients of polarization conversion R_{21} are close to zero and can be neglected. Both the resonators 1 and 2 can be strongly excited by the external field to generate resonances, corresponding to their resonance valleys and resonance peaks in the transmission spectrum T_{11} and the reflection spectrum R_{11}. In contrast, the VO_2 structure cannot be directly excited by incident waves. Therefore, the resonators 1 and 2 are bright modes, and the VO_2 structure is called a dark mode. We can see that the absorption spectra of all these structures do not have strong absorption peaks as shown in Fig. 10. This indicates that the EIA phenomenon in Fig. 10 is the result of the combined effect of all the structures. Next, the coherent phase length phenomenon of different excitation paths in the EIA structure will be illustrated by the distribution of electric field distributions.

As demonstrated in Fig. 11a, it is clearly indicated that at 0.332 THz for the EIA structure, a strong electric field can be observed on the resonator 1. This means that the resonator 1 couples stronger energy when the waves are incident on the model. However, it can be seen from Fig. 11c that at 0.532 Thz the electric field is mainly concentrated on the resonator 2 and the VO_2 structure. Therefore, it can be concluded that the resonator 1, the resonator 2 and VO_2 structure can be effectively coupled when they are concentrated together, which makes the original destructive interference into the constructive interference, producing the EIA phenomenon with the maximum absorption peak reaching above 0.9 at 0.432 THz as shown in Fig. 11b. The deeper reason for the EIA phenomenon is the magnetic effect of the magnetic dipole generated by the MS in the coupling process [48].

In the process of model optimization, we improved the frequency difference between EIT and EIA by adding air columns, reducing it from

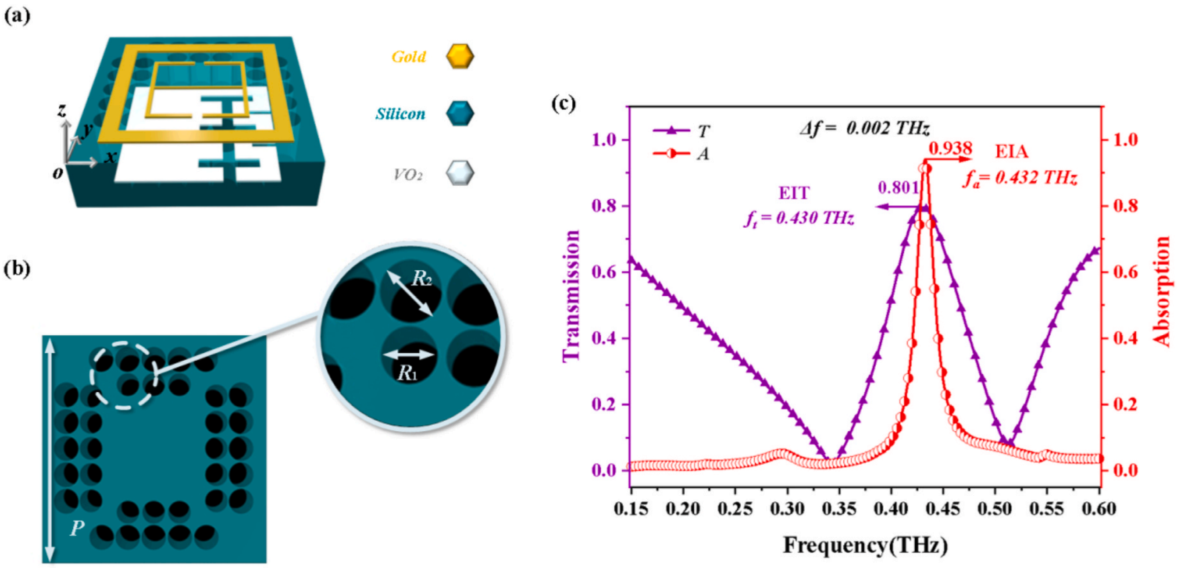

Fig. 9. (a)The structure III, (b)the silicon structure with air columns, (c) the transmission curve (*T*) of the model when VO_2 is in the insulating state and the absorption curve (*A*) of the model when VO_2 is in the metallic state.

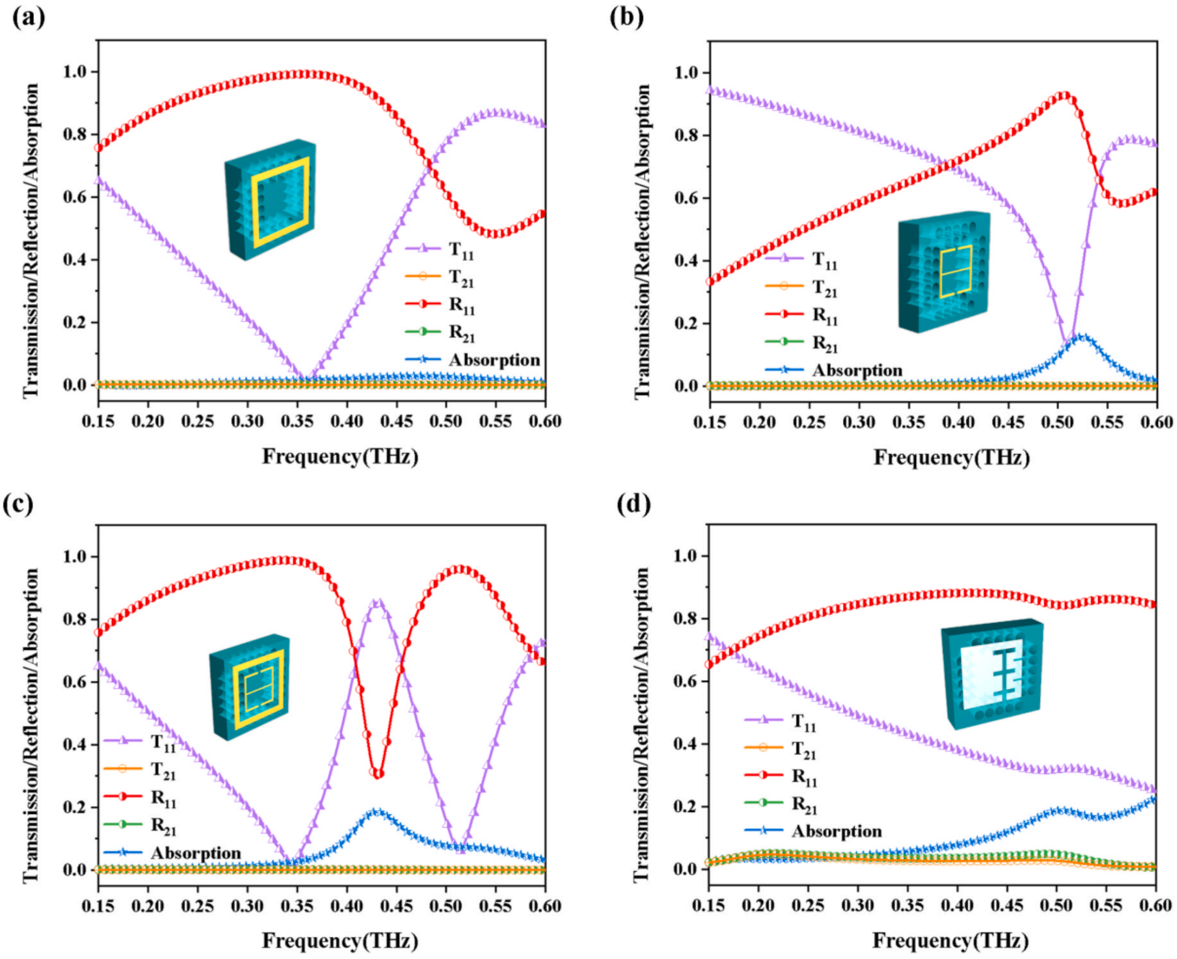

Fig. 10. The simulation of transmission, reflection and absorption spectra.(a) the resonator 1,(b) the resonator 2,(c) the combination of the resonator 1 and 2, (d) the VO_2 structure.

0.041 THz in structure II to 0.002 THz in structure III. Fig. 12 exhibits the electric field distribution of structure II and structure III. It is not difficult to find that in structure III, the electric field energy is significantly enhanced where the air column is added. Since the added air column can gather the energy and thus make the resonant frequency change, which in turn changes the frequency difference between EIT and

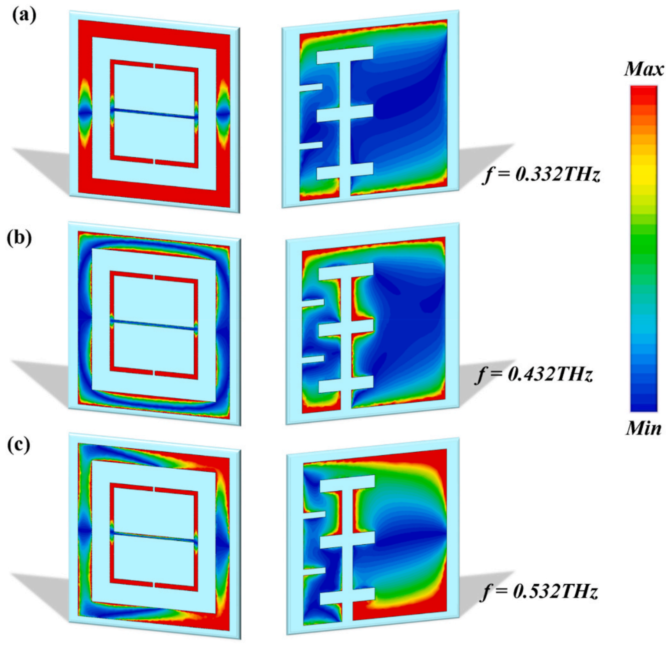

Fig. 11. Electric field distributions (EFDs) at (a) 0.332 THz,(b) 0.432 THz, and (c) 0.532 THz when the VO_2 film is in metallic state.

EIA.

Similarly, a classical four-level atomic system is used to further physically elaborate and explain the EIA behavior [7]. The four-energy level system in Fig. 13 consists of simply merged ground state energy levels |1> and |3>, and simply merged excited state energy levels |2 > and |4>. In contrast to EIT, here not only coupling light and detection light are needed for coupling and detection of EIA, but also additional control light is needed to make the jump from energy level |3> to energy level |<4. Ω_1, Ω_2, and Ω_3 in Fig. 13 are the Rabi frequencies (When an atom is irradiated by a beam of coherent light, it will periodically absorb photons and re-emit them by stimulated emission. Such a period is called the Rabi period, and its reciprocal is called the Rabi frequency.) of the coupling, probing, and control light, respectively. γ_1, γ_2, and γ_3 represent the rates at which the states of the three leap channels change, respectively. When the Rabi frequencies of the coupling field, the control field, and the decay rate of the fourth simplex energy level do not coincide, the atomic coherence process of the four-energy atomic system has different effects on the medium absorption so that the atomic coherence on the absorption is converted from phase destructive interference to phase constructive interference which is also known as EIT to EIA. The resonator 1 in the designed MS corresponds to the jump from energy level | 1> to energy level |2> in Fig. 13, and the resonator 2 corresponds to the jump from energy level |2> to energy level |3>. The VO_2 structure in the metallic state corresponds to the jump from energy level |3> to energy level |4>. The constructive interference between different excitation paths eventually contributes to the EIA phenomenon.

3. Physical mechanism and parameter discussion

3.1. The physical mechanism of the EIT and EIA phenomena

For a deep insight into the physical mechanism of the EIT behavior, the classic “dual harmonic oscillator” coupling model was utilized to explain. The interaction between the two oscillators and the incident electric field $E(t) = E_0(t)e^{-j\omega t}$ (the j means imaginary unit) can be expressed by the following differential equations [49]:

$$x_1(t)^{\bullet\bullet} + \gamma_1 \dot{x}_1\ (t) + {\omega_0}^2 x_1(t) + \Omega^2 x_2(t) = gE \tag{1}$$

$$x_2(t)^{\bullet\bullet} + \gamma_2 \dot{x}_2\ (t) + (\omega_0 + \delta) x_2(t) + \Omega^2 x_1(t) = 0 \tag{2}$$

where γ_1 and γ_2, x_1 and x_2 represent the damping and resonance amplitudes of the two oscillators, respectively. ω_0 and $\omega_0 + \delta$ denote the resonant frequencies of the two different resonators, where δ is the detuning factor, which represents the frequency difference between the transparency frequency and the resonance frequency of the intrinsic oscillators. Besides, Ω refers to the coupling strength between the two oscillators and g is the coupling strength of the bright resonator to the external field. To solve the coupled equations, the displacements vectors

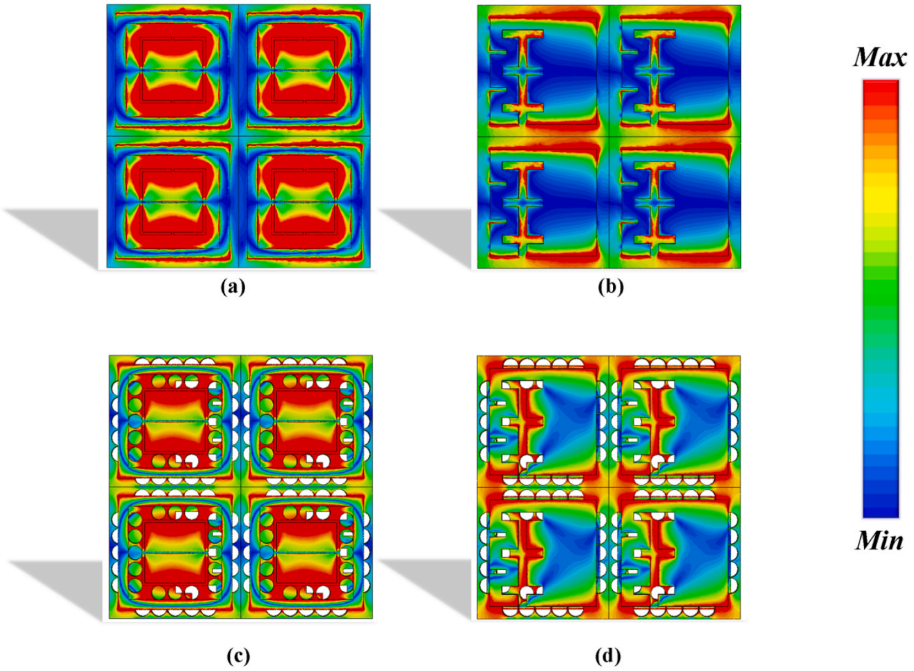

Fig. 12. The top view(a) and the bottom view(b) of electric field distributions of the structure II at 0.432 THz when the VO_2 film is in metallic state. The top view (c) and the bottom view(d) of electric field distributions of the structure III at 0.432 THz when the VO_2 film is in metallic state.

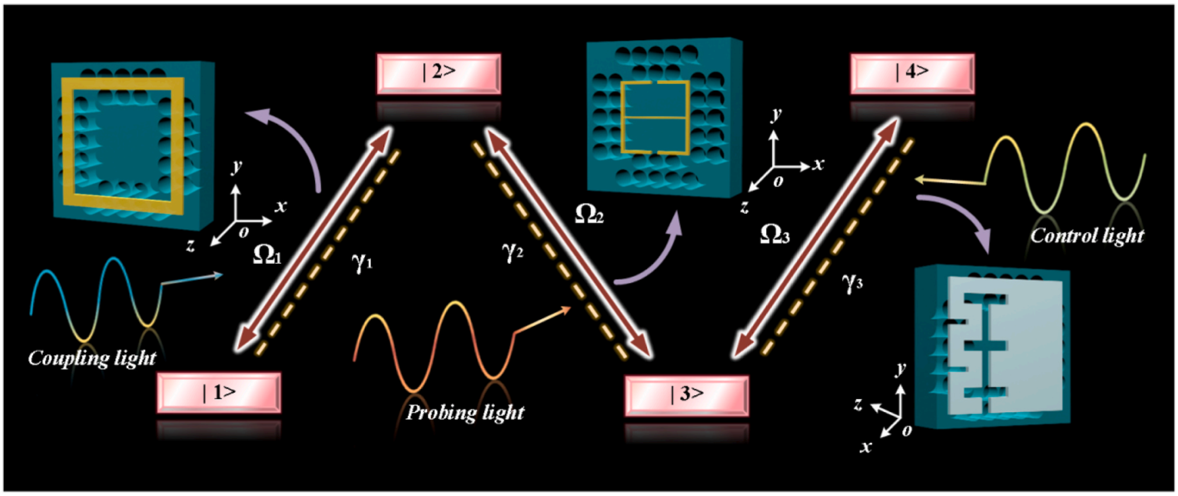

Fig. 13. The classical four-level atomic system of the EIA phenomenon in this structure.

are expressed as $x_n = C_n e^{-j\omega t}(n = 1, 2)$ and with the assistance of the approximation of $\omega_0{}^2 - \omega^2 \approx -2\omega_0(\omega - \omega_0)$, the transmission can be described as below:

$$T = 1 - \mathrm{Re}\left[\frac{jg^2(\omega - \omega_0 - \delta + j\gamma_2/2)}{(\omega - \omega_0 + j\gamma_1/2)(\omega - \omega_0 - \delta + j\gamma_2/2) - \Omega^2/4}\right] \tag{3}$$

"Re" means the real part. Using MATLABR2021b to fit the curve to the EIT, the following fitting parameters were finally obtained: $\gamma_1 = 2.2$, $\gamma_2 = 0.1$, $\Omega = 1$, $\delta = 0.007$, $\omega_0 = 2.71$, $g = 1.05$. From Fig. 14a, it can be seen that the curve fitted by equation (3) matches well with the original EIT curve.

Equally, the corresponding absorbance based on the coupled equations (1) and (2) can be gained as follows [50]:

$$A(\omega) = \frac{jg^2\omega\left(\omega^2 + j\omega\gamma_2 - (\omega_0 + \delta)^2\right)}{(\omega^2 + j\omega\gamma_1 - \omega_0{}^2)\left(\omega^2 + j\omega\gamma_2 - (\omega_0 + \delta)^2\right) - \Omega^2} \tag{4}$$

Next, with the approximation of $\omega_0{}^2 - \omega^2 \approx -2\omega_0(\omega - \omega_0)$, equation (4) can be written as:

$$A(\omega) = \mathrm{Re}\left[\frac{jg^2(\omega - \omega_0 - \delta + j\gamma_2/2)}{(\omega - \omega_0 + j\gamma_1/2)(\omega - \omega_0 - \delta + j\gamma_2/2) - \Omega^2/4}\right] \tag{5}$$

where "Re" stands for the real part. As with EIT, MATLAB was used for curve fitting, and the EIA fitting parameters were acquired as follows: $\gamma_1 = 0.17$, $\gamma_2 = 0.15$, $\delta = 0.002$, $\omega_0 = 2.72$, $g = 0.283$. The results of the EIA curve fitting are shown in Fig. 14b. It has to be noted that the fitted and simulated curves will be slightly different due to some coupling losses.

3.2. Parameter discussions

3.2.1. The parameters r_1 and r_2 discussions

As mentioned above, the EIT and EIA frequency differences do decrease after the addition of air columns arranged according to certain rules around the silica substrate. Therefore, it is necessary to discuss the parameters of the air columns for a deeper understanding. It is worth noting that the number of air columns also has some influence on the generation of the phenomenon. Only the radii of the inner and outer air columns are discussed here, while the number and arrangement of the air columns are not explained in detail here. Assume that the radii corresponding to the diameters R_1 and R_2 are r_1 and r_2, respectively. When the radius r_1 of the inner air column is varied in the range of 2175 nm–8700 nm and the radius of the outer air column r_2 is zero, it can be seen from Fig. 15a and b that both EIA and EIT resonant frequency points move in a pattern of right with the increase of r_1. As r_1 increases from 2175 nm to 8700 nm, the frequency difference between the two decreases from 0.044 THz to 0.025 THz. Next, when changing the outer column radius r_2, it can be seen from Fig. 15c and d that when r_2 is increased from 2375 nm to 9500 nm, both the EIA and EIT curves are shifted to the left. The EIA resonant frequency point shifts from 0.430

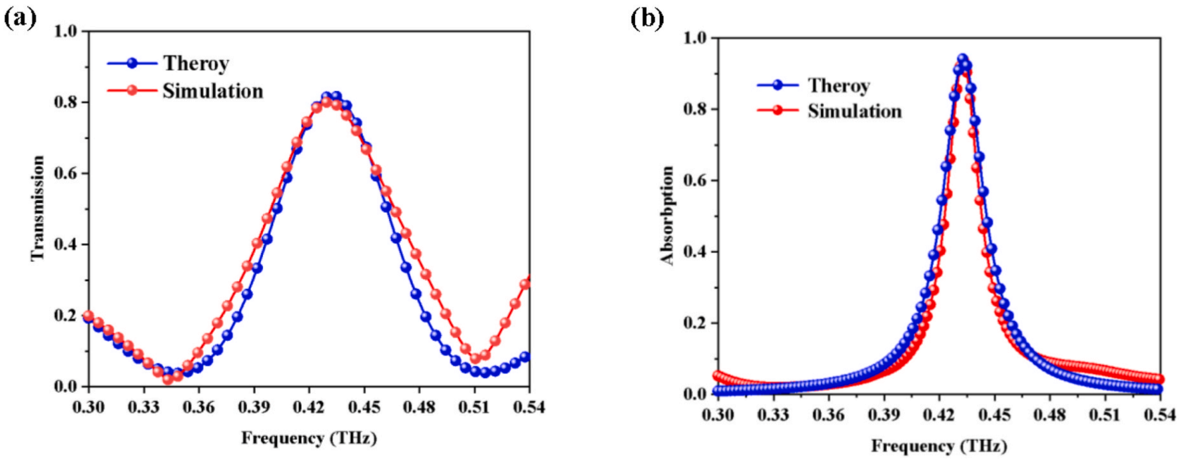

Fig. 14. The comparison of the analytically calculated values and the simulated transmission curves under the two harmonic oscillator model about (a) the EIT behavior and (b) EIA phenomenon.

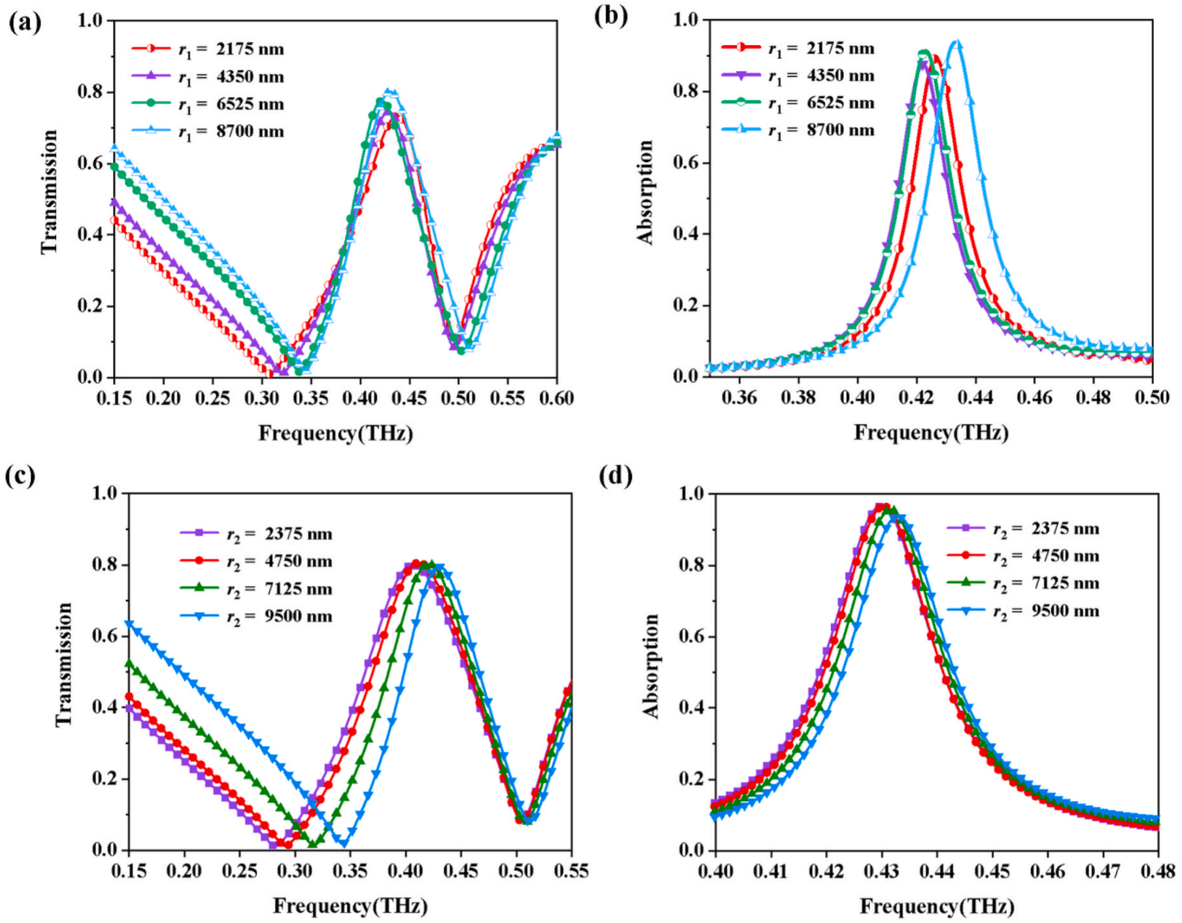

Fig. 15. The EIT (a) and EIA (b) behavior of the structure with r_1 changing from 2175 to 8700 nm ($r_2 = 0$ nm). The EIT (c) and EIA (d) phenomenon of the model with r_2 changing from 2375 to 9500 nm ($r_1 = 8700$ nm).

THz to 0.432 THz, while the EIT resonant frequency point shifts from 0.405 THz to 0.430 THz. During the increase of r_2, the frequency difference between the resonance points of EIA and EIT is decreasing. When r_2 increases to the maximum value of 9.500 μm, the frequency difference between EIT and EIA is 0.02 THz, which is a better phenomenon. Table 3 shows the variation of the peak frequency difference between EIA and EIT when the parameters r_1 and r_2 are changed.

3.2.2. *The effects of different incidence angles and polarization angles on the MS*

Last but not least, the EIT and EIA behaviors at different incidence and polarization angles are studied. Fig. 16 shows the transmission and absorption spectra when the incident electromagnetic wave is not incident perpendicular to the surface of the structure but at a certain angle of θ incidence. The angle of incidence θ is defined as the angle between the electromagnetic wave and the z-axis. From Fig. 16a, it can be observed that when the incident angle θ gradually increases from 0° to 60°, the peak of the EIT window decreases and the frequency point at the peak moves towards the lower frequency. And the same is true for the EIA behavior in Fig. 16b. It is evident that EIT and EIA exhibit instability for different incidence angles, which indicates that the MS is sensitive to the angle of incidence. The angle of polarization refers to the angle of deflection of the electric field vector of the electromagnetic wave. In Fig. 17a and b, it can be seen that while the polarization angle α changes from 0° to 90°, the EIT and EIA phenomena eventually decay or even disappear. That is to say, the EIT and EIA responses are strongly dependent on the angle of polarization.

Table 3
The change of EIT and EIA frequency differences with the changed r_1 and r_2.

r_1 (nm)	r_2 (nm)	The peak frequency of EIT (THz)	The peak frequency of EIA (THz)	Δf (THz)
0	0	0.329	0.370	0.041
2175	0	0.335	0.379	0.044
4350	0	0.349	0.392	0.043
6525	0	0.371	0.408	0.037
8700	0	0.404	0.429	0.025
8700	3375	0.405	0.430	0.025
8700	4750	0.412	0.430	0.018
8700	7125	0.421	0.432	0.011
8700	9500	0.430	0.432	0.002
0	9500	0.355	0.376	0.021

4. Conclusion

In summary, a multifunctional switchable THz MS based on phase-transition VO_2 is designed in this work. The EIT behavior of the MS can be achieved with the peak of 0.801 at 0.430 THz when VO_2 is in the temperature of 25 °C corresponding to its insulating state. When the temperature is raised from 25 °C to 68 °C, the conductivity of VO_2 will be sharply increased from 200 S/m to 300,000 S/m, which results in its state transformed from the insulating state to the metallic state. Consequently, the function of MS is converted from EIT into EIA with a strong absorption peak of 93.8 % at 0.432 THz. Furthermore, atomic energy level theory systems and classical spring oscillator model are taken for the analysis and simulation of EIT and EIA. Air column addition was performed to improve the results. This design controls the VO_2 conductivity by changing the temperature so as to realize the switching

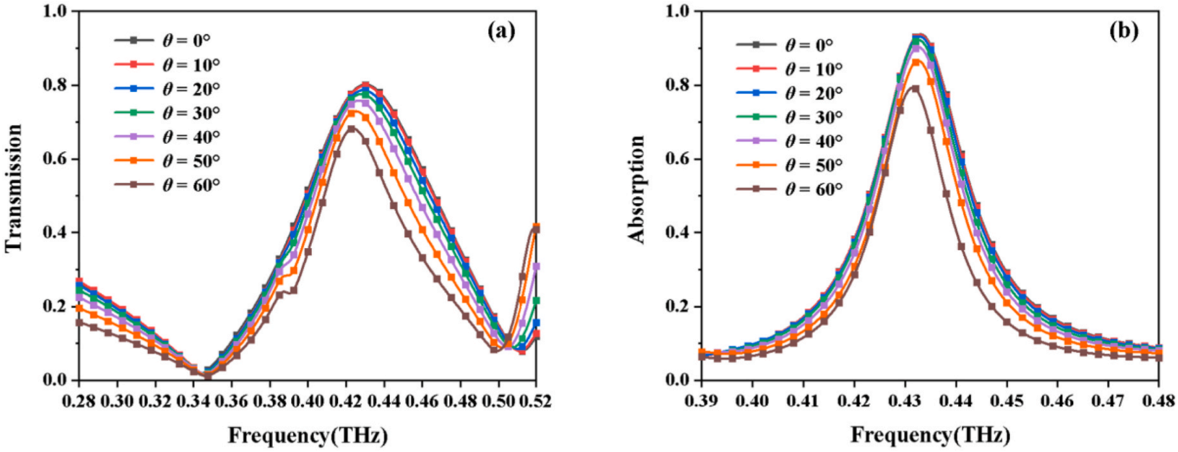

Fig. 16. (a)The EIT transmission responses with different incidence angle θ varying from 0° to 60° when the VO_2 is in the insulating state, (b)The EIA absorption spectra with different incidence angle θ varying from 0° to 60° when the VO_2 is in the metallic state.

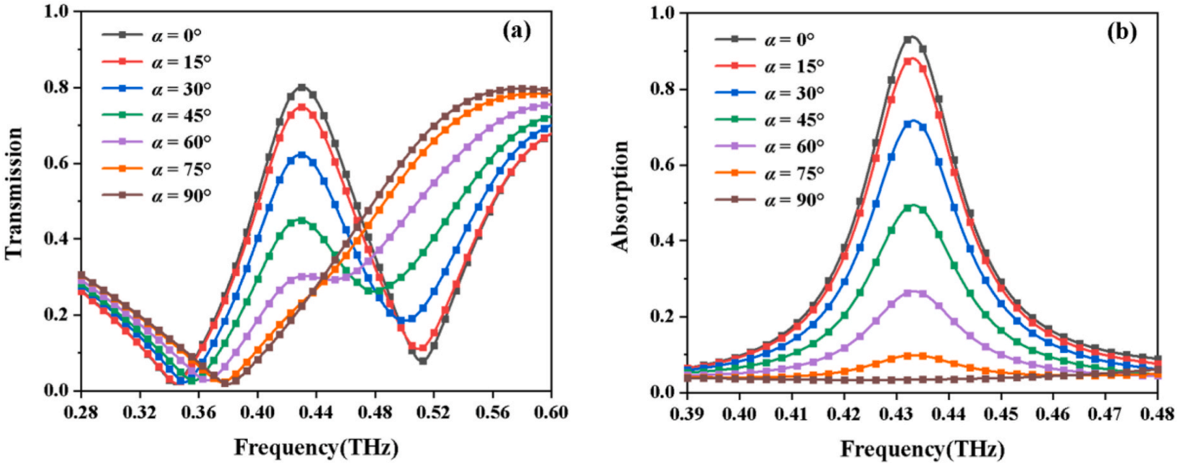

Fig. 17. (a) The EIT transmission responses with different polarization angle α varying from 0° to 90°, (b) The EIA absorption spectra with different polarization angle α varying from 0° to 90°.

of MS functions, providing ideas for the implementation of non-contact regulation technology and multi-functional reconfigurable technology. This design will have good prospects for applications in the antenna field, satellite communication technology, non-contact modulation technology, and multifunctional THz devices.

Credit authors statement

Ru-Jia Cao: Data curation, Formal analysis, Investigation. **Zhen Qiao, You Lv**: Writing - original draft, Visualization. **Hai-Feng Zhang (Corresponding author)**: Conceptualization, Methodology, Supervision, Writing - review&editing; Hai-Feng Zhangis the Corresponding author, and the email address is hanlor@163.com and hanlor@njupt.edu.cn.

Declaration of competing interest

We would like to submit the manuscript entitled “Switchable multifunctional meta-structure employing vanadium dioxide in the terahertz range”, which we wish to be considered for publication in this Journal. No conflict of interest exists in the submission of this manuscript, and the manuscript is approved by all authors for publication. I would like to declare on behalf of my co-authors that the work described was original research that has not been published previously, and not under consideration for publication elsewhere, in whole or in part. All the authors listed have approved the manuscript that is enclosed.

Data availability

Data will be made available on request.

References

[1] G. Lee, S.J. Kim, Y. Roh, S.H. Lee, D.S. Kim, S.W. Kim, M. Seo, Effective terahertz shielding properties of extreme graphene-silver nanowire surfaces investigated by nanoprobing, iScience 25 (4) (2022) 104033.
[2] R.Y. Zhou, C. Wang, Y.X. Huang, K. Huang, Y.L. Wang, W.D. Xu, L.J. Xie, Y.B. Ying, Label-free terahertz microfluidic biosensor for sensitive DNA detection using graphene-metasurface hybrid structures, Biosens. Bioelectron. 188 (2021) 113336.
[3] Y. Kawashima, S. Masaaki, K. Kuyama, T. Sakai, Y. Hayakawa, T. Kaneda, N. Sei, Terahertz imaging for formalin fixed malignant liver tumors using two-band beamline at the accelerator facility of nihon university, Appl. Sci. 12 (4) (2022) 2229.
[4] S.I. Hakeem, Z.A. Hassoun, Skin cancer detection based on terahertz images by using gabor filter and artificial neural network, IOP Conf. Ser. Mater. Sci. Eng. 928 (3) (2020).
[5] N. Arora, S.H. Gupta, B. Kumar, Performance analysis of terahertz communication link for cooperative wireless body area network, Optik 242 (2021) 167376.
[6] S.M. Sabery, A. Bystrov, M. NavarroCía, P. Gardner, M. Gashinova, Study of low terahertz radar signal backscattering for surface identification, Sensors 21 (9) (2021) 2954.

[7] D.D. Zhu, Y. Lv, S.Y. Li, H.F. Zhang, Broadband plasmon-induced transparency to a electromagnetically induced absorption conversion metastructure based on germanium, Ann. Phys. 535 (1) (2023), 2200425.

[8] R.S. Kshetrimayum, A brief intro to metamaterials, IEEE potentials 23 (5) (2004) 44–46.

[9] J.P. Marangos, Electromagnetically induced transparency, J. Mod. Opt. 45 (3) (1998) pp471–503.

[10] G. Heinze, C. Hubrich, T. Halfmann, Stopped light and image storage by electromagnetically induced transparency up to the regime of one minute, Phys. Rev. Lett. 111 (3) (2013), 033601.

[11] C. Monroe, Quantum information processing with atoms and photons, Nature 416 (6877) (2002) pp238–246.

[12] V. Giovannetti, S. Lloyd, L. Maccone, Quantum metrology, Phys. Rev. Lett. 96 (1) (2006), pp010401.

[13] S. Zhang, D.A. Genov, Y. Wang, M. Liu, X. Zhang, Plasmon-induced transparency in metamaterials, Phys. Rev. Lett. 101 (4) (2008), pp047401.

[14] J.Q. Wang, B.H. Yuan, C.Z. Fan, J.N. He, P. Ding, Q.Z. Xue, E.J. Liang, A novel planar metamaterial design for electromagnetically induced transparency and slow light, Opt Express 21 (21) (2013) 25159–25166.

[15] H.M. Li, S.B. Liu, S.Y. Liu, S.Y. Wang, G.W. Ding, H. Yang, Z.Y. Yu, H.F. Zhang, Low-loss metamaterial electromagnetically induced transparency based on electric toroidal dipolar response, Appl. Phys. Lett. 106 (8) (2015), pp083511.

[16] L.K. Foong, M. Shabani, A. Sharghi, R. Reihanisaransari, M. Al-Bahrani, B.N. Le, A. Khalilian, Electromagnetically induced transparency for efficient optical modulation in a graphene-dielectric metasurface with surface roughness, Surface. Interfac. 35 (2022) 102423.

[17] L. Gao, C. Feng, Y.F. Li, X.H. Chen, Q.P. Wang, X. Zhao, Actively controllable terahertz metal–graphene metamaterial based on electromagnetically induced transparency effect, Nanomaterials 12 (20) (2022) 3672.

[18] Q. Li, H. Su, J. Zhu, S. Wang, Active control of dual electromagnetically induced transparency in terahertz graphene-metal hybrid metasurfaces, Frontiers in Materials 9 (2022) 966535.

[19] L. Zhu, M.X. Rong, H.D. Li, L. Dong, High-sensitivity metamaterial sensor based on electromagnetically induced transparency (EIT) effect, Laser Phys. 32 (11) (2022) 116203.

[20] Y.Z. Sun, D. Zhang, H.F. Zhang, Tailoring dual-band electromagnetically induced transparency with polarization conversions in a dielectric-metal hybrid metastructure, Opt Express 30 (17) (2022) 30574–30591.

[21] M. Wan, Y. Song, L. Zhang, F. Zhou, Broadband plasmon-induced transparency in terahertz metamaterials via constructive interference of electric and magnetic couplings, Opt Express 23 (2015) 27361.

[22] J. He, P. Ding, J. Wang, C. Fan, E. Liang, Ultra-narrow band perfect absorbers based on plasmonic analog of electromagnetically induced absorption, Opt Express 23 (2015) pp6083.

[23] M.Y. Cao, T.L. Wang, H.Y. Zhang, Y.P. Zhang, Tunable electromagnetically induced absorption based on graphene, Opt Commun. 413 (2018) pp73–79.

[24] N.F. Zhong, Q.F. Dai, R.S. Liang, X.P. Li, X.P. Tan, X.M. Zhang, Z.C. Wei, F. Q. Wang, H.Z. Liu, H.Y. Meng, Analogue of electromagnetically induced absorption with double absorption windows in a plasmonic system, PLoS One 12 (6) (2017), e0179609.

[25] R.X. Ning, J. Bao, Z.H. Chen, Z. Jiao, Electromagnetically induced absorption in metamaterials and applications in the infrared range, J. Electron. Mater. 48 (2019) 4733–4739.

[26] H.Q. Dong, C.J. Gao, L. Zeng, D. Zhang, H.F. Zhang, Investigating on the electromagnetically induced absorption metamaterial in the terahertz region realized by the multilayer structure, Phys. B Condens. Matter 639 (2022) 413936.

[27] Y. Lv, D.D. Zhu, Y.Z. Sun, D. Zhang, H.F. Zhang, Transition from electromagnetically induced transparency to electromagnetically induced absorption utilizing phase-change material vanadium dioxide based on circularly polarized waves, Phys. E Low-dimens. Syst. Nanostruct. 145 (2023) 115507.

[28] M.K. Liu, H.Y. Hwang, H. Tao, A.C. Strikwerda, K. Fan, G.R. Keiser, A.J. Sternbach, K.G. West, S. Kittiwatanakul, J.W. Lu, S. Wolf, F.G. Omenetto, X. Zhang, K. Nelson&R. Averitt, Terahertz-field-induced insulator-to-metal transition in vanadium dioxide metamaterial, Nature 487 (2012) pp345–348.

[29] H.R. He, X.J. Shang, L. Xu, J.J. Zhao, W.Y. Cai, J. Wang, C.J. Zhao, L.L. Wang, Thermally switchable bifunctional plasmonic metasurface for perfect absorption and polarization conversion based on VO_2, Opt Express 28 (4) (2020) 4563–4570.

[30] D.J. Park, J.H. Shin, K.H. Park, H.C. Ryu, Electrically controllable THz asymmetric split-loop resonator with an outer square loop based on VO_2, Opt Express 26 (13) (2018) 17397–17406.

[31] X.M. Tian, Z.Y. Li, An optically-triggered switchable mid-infrared perfect absorber based on phase-change material of vanadium dioxide, Plasmonics 13 (2018) 1393–1402.

[32] T.L. Wang, H.Y. Zhang, Y. Zhang, Y.P. Zhang, M.Y. Cao, Tunable bifunctional terahertz metamaterial device based on Dirac semimetals and vanadium dioxide, Opt Express 28 (12) (2020) 17434–17448.

[33] M.M. Chen, Z.Y. Xiao, X.J. Lu, F. Lv, Z.T. Cui, Q.D. Xu, Dynamically tunable multi-resonance and polarization-insensitive electromagnetically induced transparency-like based on vanadium dioxide film, Opt. Mater. 102 (2020), 109811.

[34] Z.Y. Liu, L.M. Qi, J. Ahmed Uqaili, J. Yang, X. Tao, D.D. Sun, C.W. Lan, A Multi-functional terahertz metamaterial with polarization-controlled EIT and broadband absorption, Mod. Phys. Lett. B 36 (21) (2022), 2250099.

[35] X.K. Li, S.W. Tang, F. Ding, S.M. Zhong, Y.Q. Yang, T. Jiang, J. Zhou, Switchable multifunctional terahertz metasurfaces employing vanadium dioxide, Sci. Rep. 9 (1) (2019) 5454.

[36] D.C. Wang, S. Sun, Z. Feng, W. Tan, Enabling switchable and multifunctional terahertz metasurfaces with phase-change material, Opt. Mater. Express 10 (9) (2020) 2054–2065.

[37] S. Mallick, D.R. Chowdhury, Broadside-coupling–enabled insulator-to-metal transition in a terahertz metasurface, Europhys. Lett. 138 (5) (2022).

[38] Y.Z. Sun, Z.H. Guo, C.J. Gao, H.F. Zhang, Tunable polarization comb based on the electromagnetically induced transparency with hybrid metal-graphene metamaterial, Phys. Scripta 96 (12) (2021).

[39] R. Yahiaoui, M. Manjappa, Y.K. Srivastava, R. Singh, Active control and switching of broadband electromagnetically induced transparency in symmetric metadevices, Appl. Phys. Lett. 111 (2) (2017).

[40] T.T. Lv, Y.X. Li, H.F. Ma, Z. Zhu, Z.P. Li, C.Y. Guan, J.H. Shi, H. Zhang, T.J. Cui, Hybrid metamaterial switching for manipulating chirality based on VO_2 phase transition, Sci. Rep. 6 (1) (2016) pp.1–9.

[41] B.G. Chae, D.H. Youn, H.T. Kim, S.Y. Maeng, K.Y. Kang, Fabrication and electrical properties of pure VO_2 phase films, 2003, 0311616.

[42] L. Zhang, P. Tassin, T. Koschny, C. Kurter, S.M. Anlage, C.M. Soukoulis, Large group delay in a microwave metamaterial analog of electromagnetically induced transparency, Appl. Phys. Lett. 97 (24) (2010), 241904.

[43] X.R. Jin, J. Park, H.Y. Zheng, S. Lee, Y. Lee, J.Y. Rhee, K.W. Kim, H.S. Cheong, W. H. Jang, Highly-dispersive transparency at optical frequencies in planar metamaterials based on two-bright-mode coupling, Opt Express 19 (22) (2011) pp21652–21657.

[44] Li Hai ming, Feng Xue, Comparing Q-factor of electromagnetically induced transparency based on different space distribution quasi-dark mode resonator, J. Appl. Phys. 122 (4) (2017).

[45] V.A. Fedotov, M. Rose, S.L. Prosvirnin, N. Papasimakis, N.I. Zheludev, Sharp trapped-mode resonances in planar metamaterials with a broken structural symmetry, Phys. Rev. Lett. 99 (14) (2007), pp147401.

[46] H.Y. Zhang, Y.Y. Cao, Y.Z. Liu, Y. Li, Y.P. Zhang, A novel graphene metamaterial design for tunable terahertz plasmon induced transparency by two bright mode coupling, Opt Commun. 391 (2017) 9.

[47] C.X. Liu, Y.L. Xu, H.Q. Liu, M.T. Lin, S. Zha, Switchable metamaterial with terahertz buffering and absorbing performance, IEEE Photon. J. 13 (5) (2021) pp1–8.

[48] X.Q. Zhang, N.N. Xu, K.N. Qu, Z. Tian, R.J. Singh, J.G. Han, Girish S. Agarwal, W. L. Zhang, Electromagnetically induced absorption in a three-resonator metasurface system, Sci. Rep. 5 (1) (2015) 10737.

[49] H. Lin, D. Yang, S. Han, Y.J. Liu, H.L. Yang, Analog electromagnetically induced transparency for circularly polarized wave using three-dimensional chiral metamaterials, Opt Express 24 (2016) pp30068–30078.

[50] C.J. Gao, H.F. Zhang, Switchable metasurface with electromagnetically induced transparency and absorption simultaneously realizing circular polarization-insensitive circular-to-linear polarization conversion, Ann. Phys. 534 (7) (2022), pp2200108.